Photoluminescence of GaAs/$Al_xGa_{1-x}As$ multiple quantum well structures containing δ-doping superlattices

S. M. Landi,* C. V.-B. Tribuzy, P. L. Souza, and R. Butendeich†
LabSem, CETUC, Pontifícia Universidade Católica, Rua Marquês de São Vicente 225, Rio de Janeiro, 22453-900 Brazil

A. C. Bittencourt and G. E. Marques
Departamento de Física, Universidade Feferal de São Carlos, 13565-905 São Carlos, São Paulo, Brazil
(Received 28 December 2001; revised manuscript received 26 August 2002; published 5 February 2003)

GaAs/$Al_xGa_{1-x}As$ multiple quantum well structures containing *nipi*-δ-doping superlattices were grown by low-pressure-metalorganic vapor phase epitaxy. Optical properties of such structures have been studied by photoluminescence (PL) as a function of temperature and incident excitation power. A critical temperature, below which PL emissions come from spatially indirect transitions, is defined. The indirect transitions occur between levels inside the GaAs quantum well (QW) and inside the inverted V-shape potential in the $Al_xGa_{1-x}As$ barriers. Above the critical temperature, a direct transition, which involves levels only inside the GaAs QW, is the dominant transition in the PL spectra. Theoretical calculations helped to understand the PL peak energy behavior with temperature and confirmed the indirect character of the emissions below the critical temperature. The indirect character was also identified through PL measurements as a function of the incident excitation power. The dependence of the critical temperature both on the samples' structure and on the incident excitation power is discussed.

DOI: 10.1103/PhysRevB.67.085304 PACS number(s): 78.55.Cr, 73.21.−b

I. INTRODUCTION

Experimental research on *nipi* structures started to receive attention in the 1980's.[1,2] The first structures were grown in bulk materials with *n*- and *p*- doped periodic layers hundreds of angstroms wide, separated by an intrinsic zone.[1–4] In these structures, the impurity layers give rise to an oscillating potential which confines electrons and holes to different spatial regions. Structures where electrons and holes are spatially separated lead to long radiative recombination lifetimes and, therefore, the associated band-filling effects can be enhanced. The possibility of tuning band-gap energies and free-carrier densities was very attractive in these materials leading to tunable electronic properties such as conductivity, luminescence spectra, optical absorption, and recombination lifetimes.[3] In such *nipi* structures a blue shift of the effective band gap can be observed for increasing excitation power. Döhler *et al.*[1] have shown that this behavior occurs since the amplitude of the space-charge superlattice potential decreases with increasing carrier concentration due to the spatial separation of electrons and holes.

As the growth techniques and doping control were optimized, thinner doping layers became possible to be grown and, nowadays, the δ-doping structures with dopants confined only to a few atomic layers can be routinely obtained. Johnston *et al.*[5] have presented a systematic photoluminescence (PL) study of a δ-doped *nipi* structure consisting of Si and C δ-doped layers in GaAs. Such structure has been called a sawtooth superlattice because of the combination of the V-shape potential created by the *n*-type doping layer and of the inverted V-shape potential created by the *p*-type doping layer profile. Those authors have found interesting band-edge relaxation effects in the time resolved PL experiments, revealed by two effects, namely, a blue shift of the effective band gap with increasing excitation power and a temporal evolution of the band edges.

Bastola *et al.*[6] have formulated a quantitative dependence of the effective band gap on the excitation light intensity in an *nipi* structure and determined a logarithmic dependence between the optical blue shift and the excitation intensity. They have confirmed experimentally such behavior in $Al_xGa_{1-x}As$ *nipi* samples.

Hetero-*nipi* structures, which involves a heterostructure and *nipi*-doped layers, have been largely applied in the fabrication of phase modulators[7–9] and optically addressed spatial light modulators (O-SLM's).[10,11] The interest in the use of δ doping to produce thin *n* and *p* layers has been previously pointed out by Larsson and Maserjian.[10] For device applications where short periods are required, the thickness of each doped layer approaches the mean distance between the dopants, leading to fluctuations in the confining potential. The use of δ doping can improve these devices by reducing these potential fluctuations.

Another application of δ-doped layers is on amplitude modulators based on the quantum confined Stark effect. Such modulators require the maximization of the change in absorption per applied reverse voltage. Batty and Allsopp[12] have proposed an alternative structure in order to increase the Stark shift, where an *nipi*-δ-doping superlattice is introduced into a multiple quantum well (MQW) structure. In this work, we are reporting PL studies of the role played by the temperature, excitation power, and doping profile on MQW structures containing a δ-doping superlattice (SL). We have investigated *nipi*-δ-doping SL on GaAs/$Al_xGa_{1-x}As$ MQW, where an *n*-type δ doping is localized in the center of the GaAs quantum wells and a *p*-type δ doping is localized in the center of the $Al_xGa_{1-x}As$ barriers. The doping level has been varied, in order to verify how the optical properties change as a function of this parameter. Our study on the

 ©2003 The American Physical Society

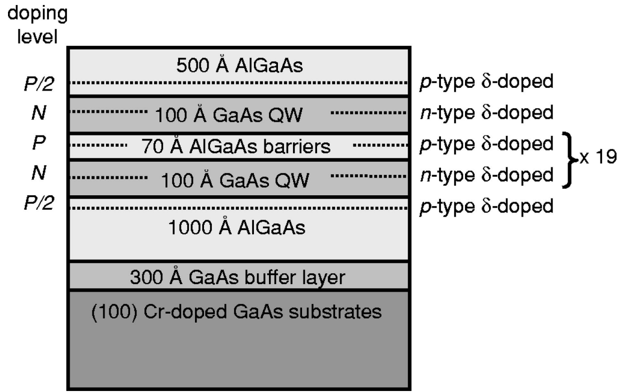

FIG. 1. Schematic view of an *nipi*-δ-doped MQW sample.

dependence of the PL on the temperature has revealed two different emission processes, whose nature are related either to the MQW structure profile or to the *nipi* character of each structure. The interpretation of the measurements has been confirmed by theoretical calculations. MQW samples with only n-δ-doping superlattices inside the GaAs QW's have also been investigated, helping us to isolate the effects coming from the presence of the p-type doping in the $Al_xGa_{1-x}As$ barriers. The article is organized as follows. In Sec. II, we describe the experimental details for sample preparation and characterization. A table containing the doping levels of the investigated samples is included. The theoretical model is outlined in Sec. III. Both theoretical and experimental results are described and discussed in Sec. IV. First, we present the results concerning the structures with only the n-δ doping superlattice, followed by those obtained for the *nipi*-δ doped superlattices. Finally, in Sec. V, we provide the conclusion.

II. EXPERIMENTAL DETAILS

The $GaAs/Al_xGa_{1-x}As$ MQW samples have been grown by metalorganic vapor phase epitaxy on (100)-oriented Cr-doped GaAs substrates. An undoped 30-nm-thick GaAs buffer has been grown on the substrate, followed by a 100-nm-$Al_{0.3}Ga_{0.7}As$ layer, before the deposition of the MQW layers. The MQW structure consists of 20 periods of 100-Å-thick GaAs quantum wells, and 70 Å-thick $Al_{0.3}Ga_{0.7}As$ barriers. The *nipi* samples were grown with a Si δ-doping layer at the center of the QW's and a C δ doping at the center of the barriers. SiH_4 and CBr_4 were used, respectively, as the n- and p-type doping precursors. A diagram of the *nipi* samples is shown in Fig. 1. A good localization of the δ layers was detected by C-V measurements. In particular, for the C doping, a systematic study was carried out to reach control of the doping level as published elsewhere.[13] Structures containing only n-δ-doped layers in the QW's, with no p-δ-doped layers, were also grown. Furthermore, undoped samples were grown with the same MQW structures as the doped ones, to serve as references. Different sheet carrier densities have been used for each sample, which are summarized in Table I. The period of the structures was measured by x ray in a Bede Scientific QC2a diffractometer.

PL measurements were carried out with the 514-nm line

TABLE I. Nominal 2D-doping levels of the samples studied.

Sample	Type	$N(10^{12}\ \mathrm{cm}^{-2})$	$P(10^{12}\ \mathrm{cm}^{-2})$
502	*nipi*	0.5	0.5
498	*nipi*	0.42	0.55
482	*nipi*	1.82	2.3
494	*n*	0.2	
480	*n*	1.7	
491	*n*	2.5	
484	undoped[a]		

[a]Reference sample.

of an Ar^+ laser for excitation. The signal was dispersed by a 250-mm monochromator and detected by a Ge nitrogen cooled photodetector. The excitation laser was chopped at 145 Hz for signal detection by standard lock-in techniques. PL experiments were performed for temperatures between 15 and 300 K, and power-excitation densities between 0.04 and 60 Wcm^{-2}.

III. THEORETICAL MODEL

The luminescence spectrum for isolated δ-like structures with n- or p-type doping concentration on bulk samples has been presented by Sipahi *et al.* using either the Luttinger[14] plus parabolic (conduction) model or the 8×8 Kane[15] model to calculate the self-consistent electronic structure. They have included the exchange-correlation effects in their calculation and used it to study the effect of temperature on the "direct"-transition luminescence spectra. The comparison with experiments required an estimate for the band-gap renormalization and the introduction of about 25% of an excess charge to decrease the theoretical calculated resonance energy in their simulation of the photoinduced excitation effects.

Here, we will be analyzing a more complex system composed of coupled multidoped layers located either inside the wells (n type) or in the barriers (p type). These spatial restrictions and couplings make it difficult to determine the exact number of ionized impurity states in each layer. Moreover, the calculation of optical transitions makes it necessary the use of $\mathbf{k}\cdot\mathbf{p}$ model in order to take into account the important couplings and mixings between the n- and p- type layers through the inherent mixing between valence-band states, as well as the coupling between valence and conduction bands, naturally present in the Kane-Hamiltonian. The closest the n- and p -doped layers are, the stronger will their interaction be. Therefore, results from self-consistent calculations on isolated n or p layers in bulk samples are not directly applicable to the present situation.

In order to study the luminescence in the *nipi*-QW structure, we have used a simple linear V-shaped confinement potential model to simulate the spatial localization of the majority carriers. They are located at the center of the n-δ-doped layer in the well and of the two lateral p-δ-doped layers in the barriers, as shown in Fig. 2. The luminescence spectrum, normalized to an intensity I_0, requires the knowl-

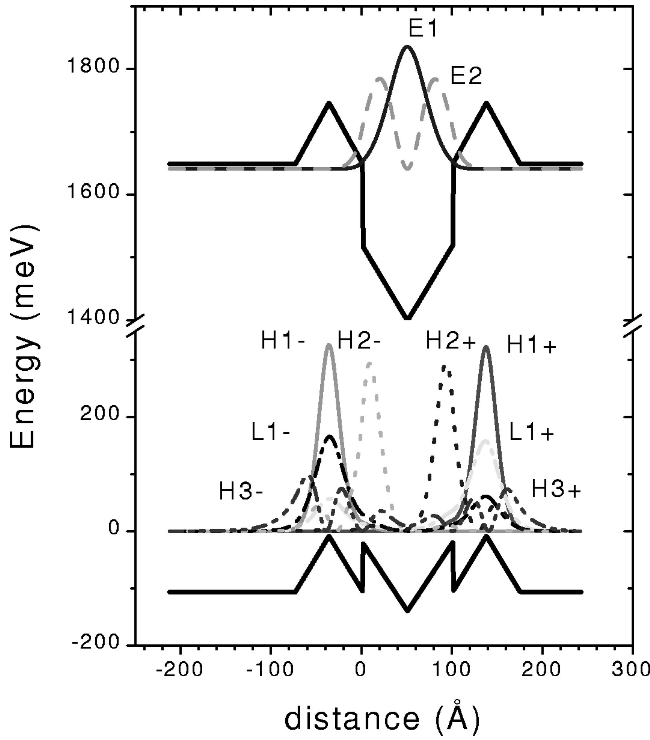

FIG. 2. The potential profile and the probability density $|\Psi_i^j(0,0,z)|^2$ for a few states in a sample. The heavy and light hole eigenstates are labeled H and L, respectively, and the electron eigenstates E. Notice that the hole states can be strictly localized in one material or be extended to the other layers, depending on the value of their energy as compared with the band offset in the heterostructure.

edge of all occupied (electrons) and empty (holes) states that can be calculated as

$$\frac{I}{I_0}=\pounds(\omega)=\sum_{\mathbf{k},n_c,n_v}\frac{\Im_{n_c}(\mathbf{k})[\mathbf{1}-\Im_{n_v}(\mathbf{k})]\mathbf{f}_{n_c,n_v}(\mathbf{k})\Gamma^2_{n_c,n_v}}{\{[E^c_{n_c}(\mathbf{k})-E^v_{n_v}(\mathbf{k})-\hbar\omega]^2+\Gamma^2_{n_c,n_v}\}},$$

where $\Im_{n_c}(\mathbf{k})$ and $[\mathbf{1}-\Im_{n_v}(\mathbf{k})]$ are the Fermi occupation probabilities for electron (with quasi-Fermi energy E_F^n) and hole (with quasi-Fermi energy E_F^p) states whose transition energy $[E^c_{n_c}(\mathbf{k})-E^v_{n_v}(\mathbf{k})]$ displays a broadening Γ_{n_c,n_v} at certain wave number $\mathbf{k}$, respectively. In general, Γ_{n_c,n_v} is assumed to be independent of $\mathbf{k}$ for recombination between levels with a set of quantum numbers n_c and n_v. Also, we have not used any possible dependence of the quasienergies of electrons and holes on the temperature. Finally, $\mathbf{f}_{n_c,n_v}(\mathbf{k})$ is the oscillator strength, for the electron-hole optical recombination of states at given $\mathbf{k}$, defined as

$$\mathbf{f}_{n_c,nv}(\mathbf{k})=\frac{1}{m_0}\sum_{n_c,n_v}\frac{|\langle\Psi_i^c(\mathbf{k},\rho,z)|p_\alpha|\Psi_j^v(\mathbf{k},\rho,z)\rangle|^2}{[E^c_{n_c}(\mathbf{k})-E^v_{n_v}(\mathbf{k})]},$$

where $\boldsymbol{\rho}=(\mathbf{x},\mathbf{y})$ $[z]$ is the in-plane [confinement] coordinate, p_α is the momentum operator for light with a given polarization, $\alpha=x,\ y,\ z$, that must be chosen according to the selection rules for optical transition between the initial $[|\Psi_i^c(\mathbf{k},\rho,z)\rangle]$ and the final $[|\Psi_j^v(\mathbf{k},\rho,z)\rangle]$ states in the conduction and valence bands, respectively.

For potential profiles with inversion symmetry with respect to the z coordinate, the spin-up and spin-down Kramer doublets are strictly degenerate and leading to a factor of 2 in the above sums. Any spatial asymmetry, such as the one induced by an uniform electric or magnetic field, will lift the Kramer degeneracy for all values of $\mathbf{k}\neq 0$. Thus, for a perfect *nipi* sample, where the two p layers and the n layer have an inversion symmetry with respect to center of the well, the Kramer doublets will remain degenerate at all values of $\mathbf{k}$. Any spatial asymmetry makes the states lose their invariance under the time-reversal operator, $\check{\mathbf{T}}=-i\hat{\sigma}_y\ \hat{\mathbf{C}}\ \hat{\mathbf{I}}$, where $\hat{\sigma}_y$ is the Pauli spin matrix, $\hat{\mathbf{C}}$ the complex conjugation, and $\hat{\mathbf{I}}$ the spatial inversion operators, respectively. The Kane-Hamiltonian model (kinetic energy) plus any symmetrical potential $V(z)$ will commute with $\check{\mathbf{T}}$. Furthermore, if there are s—regions of spatial confinement there will be s—levels of energy, solutions of the Schrödinger equation due to the coupling (tunneling) of states in each region. The energy separation between them changes accordingly to the tunneling probability of carriers between the regions, and this fact must be included in any calculation for an *nipi* sample. These theoretical difficulties made us avoid a self-consistent calculation. However, we have chosen a simpler profile model that would provide good insight on the trends and on the main general features observed in our experiments, as well as lead to an explanation and an understanding of the physics involved in this system.

In our non self-consistent approach the local internal electric fields were adjusted by the effective doping charge densities of each majority-carrier type in the sample, in order to produce a depth in each doping profile, in the form

$$V(z)=\left(\frac{e^2}{\kappa\epsilon_0}n_{eff}\right)z, \tag{1}$$

where κ is the dielectric constant of each undoped layer. For each type of dopant in a given sample, the effective carrier concentration n_{eff} was chosen as to produce calculated values for the conduction-band–valence-bands transition energies which would agree with the experimental PL peak energy at the lowest value of temperature $(T\sim 0)$. Thus, the position of the quasi-Fermi energies E_F^n and E_F^p are included with an estimate from known values for isolated δ-doping cases. However, it is taken into account that the eigenstates in our system may have different spatial degeneracies and multiple energy (due spatial symmetry) dispersions, besides the usual spin degeneracy. Then, the fitted profile was kept at all temperatures and all effects, due to an increase in the temperature, were assigned only to the change in the energy gap of the materials in the well and in the barrier. This linear potential approximation can give fairly good values only for the ground-state energy, clearly, it overestimates the energies of all excited states as compared to the self-consistent δ-doped potential, where the local fields decrease smoothly to zero away from the doped layer. Anyway, in the luminescence experiments, the most important transition occurs be-

tween ground states. Moreover, the determination of the real position of the quasi-Fermi levels in the present system, would require a combined experimental study of the optical absorption and of the luminescence under equal conditions. Finally, the fitting approach described above already includes the unknown values of the real band-gap renormalization of our *nipi*-QW structures and possible excitonic shift, contributions that are always present in the experiments. Yet, in the spatially indirect optical transitions the excitonic effects are well known to have a small contribution. The general aspect of the full confining potential used for the *nipi* samples is shown, qualitatively, Fig. 3(d). Notice that the presence of each type (doping) of layer has different influence on the opposite carrier type. The two lateral p layers pull electrons to the center of the quantum well, while the n layer pulls carriers towards the empty states (or filled hole states). This is an induced asymmetry for holes with respect to the center of the p layer.

The electronic states for any potential profile are calculated within the full Weiler-Kane **k·p** Hamiltonian model,[16] which has proved to be an excellent approach to the eigenvalue problem since first-principles calculation is far beyond our present purposes. The V-shape potentials for the layers are added to the flat-band quantum well profile, and then, the k-dependent solutions of $[H_{k.p}+V(z)I]\Psi_i(\mathbf{k},x,y,z) = E_i(\mathbf{k})\Psi_i(\mathbf{k},x,y,z)$, for the ith carrier type, with any spin component, are obtained. The full Hamiltonian for the chosen ordering of Bloch states Γ point ($e+$, $hh+$, $lh+$, $so+$, $e-$, $hh-$, $lh-$, $so-$) is given by

$$H_{k.p}=\begin{bmatrix} \hat{D}_{el} & \sqrt{\frac{1}{2}}\hat{L}_{+} & -\sqrt{2}\hat{P}_z & \hat{P}_z & 0 & 0 & -\sqrt{\frac{1}{6}}\hat{L}_{-} & -\sqrt{\frac{1}{3}}\hat{L}_{-} \\ & \hat{D}_{hh} & \hat{G}_{-} & -\frac{1}{\sqrt{8}}\hat{G}_{-} & 0 & 0 & \hat{W} & \hat{W} \\ & & \hat{D}_{lh} & \hat{R} & \sqrt{\frac{1}{6}}\hat{L}_{-} & \hat{W} & 0 & -\sqrt{\frac{3}{8}}\hat{G}_{-} \\ & & & \hat{D}_{so} & \sqrt{\frac{1}{3}}\hat{L}_{-} & \hat{W} & \sqrt{\frac{3}{8}}\hat{G}_{-} & 0 \\ & & & & \hat{D}_{el} & \sqrt{\frac{1}{2}}\hat{L}_{-} & -\sqrt{2}\hat{P}_z & \hat{P}_z \\ & & & & & \hat{D}_{hh} & \hat{G}_{+} & +\frac{1}{\sqrt{8}}\hat{G}_{+} \\ & & & & & & \hat{D}_{lh} & \hat{R} \\ & & & & & & & \hat{D}_{so} \end{bmatrix}. \quad (2)$$

Each term in the Hamiltonian can be written in terms of the bulk parameters for each material, in the form

$$\hat{D}_{el}=\left[E_g^0+E_\nu^c\left(|z|-\frac{L_z}{2}\right)+\left(F_0+\frac{1}{2}\right)k_\parallel^2+\left\{\hat{k}_z\left(F_0+\frac{1}{2}\right)\hat{k}_z\right\}\right];$$

$$\hat{D}_{hh}=\hat{D}^{+};\quad \hat{D}_{lh}=\hat{D}^{-},$$

$$\hat{D}^{\pm}=\left[-E_\nu^v\left(|z|-\frac{L_z}{2}\right)-\left(\frac{\gamma_1\pm\gamma_2}{2}\right)k_\parallel^2-\left\{\hat{k}_z\left(\frac{\gamma_1\mp 2\gamma_2}{2}\right)\hat{k}_z\right\}\right];$$

$$\hat{P}_z=\frac{1}{\sqrt{3}}\{P_0,\hat{k}_z\};\quad \hat{k}_z=-i\frac{\partial}{\partial z},$$

$$\hat{D}_{so}=\left[-\Delta_{so}-E_\nu^v\left(|z|-\frac{L_z}{2}\right)-\frac{\gamma_1}{2}k_\parallel^2-\left(\hat{k}_z\frac{\gamma_1}{2}\hat{k}_z\right)\right];$$

$$\hat{L}_{\pm}=P_0\hat{K}_{\pm},\quad \hat{K}_{\pm}=(k_x+ik_y);\quad \hat{G}_{\pm}=\sqrt{3}\hat{K}_{\pm}\{\gamma_3,\ \hat{k}_z\},$$

$$\hat{W}=\left[-\frac{\sqrt{3}}{2}\left(\frac{\gamma_2+\gamma_3}{2}\right)\hat{K}_{-}-\sqrt{\frac{3}{2}}\left(\frac{\gamma_2-\gamma_3}{2}\right)\hat{K}_{+}\right]$$

$$\text{and}\quad \hat{R}=\left[\sqrt{2}(\hat{k}_z\gamma_2\hat{k}_z)-\sqrt{\frac{1}{2}}\gamma_2 k_\parallel^2\right].$$

In these expressions, E_g^0 is the band gap, $E_\nu^{c(v)}$ is the band offset for conduction (valence) band, and Δ_{so} is the spin-orbit energies, for each host material. Also, θ is the angle between the components of the in-plane linear momentum vector $\mathbf{k}=(k_x,k_y)$ with modulus $k_\parallel=\sqrt{k_x^2+k_y^2}$. Moreover, $\{a,b\}=(ab+ba)/2$ is a symmetrized Hermitian form that can handle the z dependence of the well-known first ($P_0 = \langle s|\partial/\partial x|X\rangle$) and second ($\gamma_1$, γ_2, γ_3, F_0) order Kane-Luttinger-Weiler[16] parameters determining the

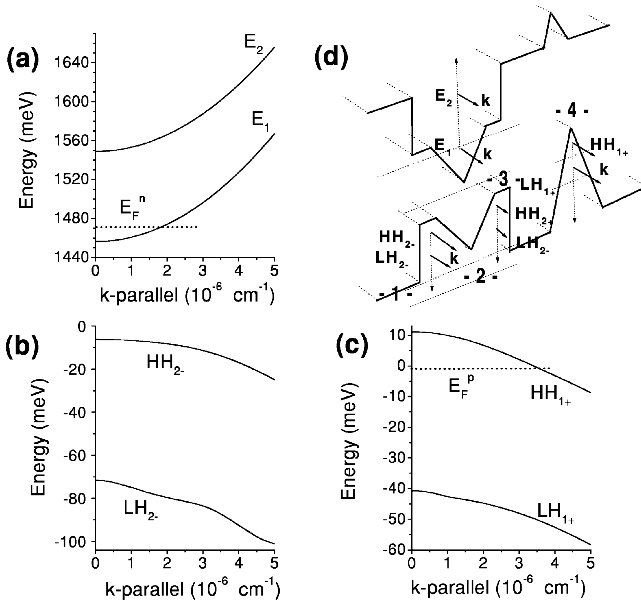

FIG. 3. Calculated energy dispersions for sample 482 at 170 K; (a) for electrons in the n-doped layer on the GaAs QW, (b) for hole states on the left part of the valence band of the GaAs QW, (c) for hole states on the right p-doped layer on the Al$_x$Ga$_{1-x}$As barrier. Part (d) shows the qualitative full confining potential used.

conduction-band–valence-band coupling and the admixture of the valence-band states in each layer of the heterostructure. All these material parameters should be measured in units of $(\hbar^2/m_o)$, m_o being the free-electron mass, and every energy is measured from the zero-energy assigned at the top of the valence band. All material parameters for GaAs and AlAs were taken from Ref. 17. The temperature dependence of the effective masses of any carrier is considered from their dependence on the gap energy (meV) for GaAs and AlAs,

$$E_g^0(T)=1519.2-0.58\left[\frac{T^2}{T+300}\right] \quad \text{(GaAs)},$$

$$E_g^0(T)=2239.0-0.60\left[\frac{T^2}{T+408}\right] \quad \text{(AlAs)},$$

respectively, and T is given in kelvin. We also assume a linear extrapolation on the concentration x to determine all band parameters in a Ga$_{1-x}$Al$_x$As layer, but any other parameter extrapolation may be used.[18] Certainly, all parameters and effective masses for a given material will depend on the temperature through $E_g^0(T)$. As a final comment, the first four spin-up Bloch states $\{|e+\rangle, |hh+\rangle, |lh+\rangle, |so+\rangle\}$ is time reversal of the set of spin-down states $\{|e-\rangle, |hh-\rangle, |lh-\rangle, |so-\rangle\}$, thus, any solution of the Kane-Hamiltonian, in any spatially symmetric potential profile, have degenerate Kramer doublets.

The ith state in the conduction band, for the chosen ordering of Bloch states Γ point, has envelope function components in all eight Bloch states, and are written in the form

$$\Psi_i^c(\mathbf{k},\rho,z)=e^{i\mathbf{k}.\rho}\begin{bmatrix} F_1^{i,c}(\mathbf{k},z) & |e+\rangle \\ F_2^{i,hh}(\mathbf{k},z) & |hh+\rangle \\ F_3^{i,lh}(\mathbf{k},z) & |lh+\rangle \\ F_4^{i,so}(\mathbf{k},z) & |so+\rangle \\ \cdots\cdots & \\ F_8^{i,so}(\mathbf{k},z) & |so-\rangle \end{bmatrix}, \qquad (3)$$

where $\rho=x,y$ is the position of the carrier in the xy plane, and $F_1^{i,c}(\mathbf{k},z)[{}_5^{i,c}(\mathbf{k},z)]$ is the z-envelope function in the spin-up (spin-down) conduction state. This example sets the notation for any other state of the system as well as its envelope function components.

The eigenstates $\{\Psi_i^c(\mathbf{k},\rho,z)\}$ and eigenenergies $\{E_i(\mathbf{k})\}$, for all wave vector $\mathbf{k}$, are calculated by using the combined finite difference and inverse power methods.[19,20] The length of the system in the z direction was divided in N grid points and each differential operator inside the Hamiltonian was written in a proper discrete form. The Schrödinger equation becomes an $8N\times 8N$ matrix, whose solutions can be put in a form

$$(\mathbb{H}-\lambda\mathbb{I})^{-m}\mathbb{F}^{(0)}(z)=\sum_{i=1}^{N}\left[\frac{a_i\mathbb{F}_i(z)}{(E_i(\mathbf{k})-\lambda)^m}\right]. \qquad (4)$$

The initial condition $\mathbb{F}^{(0)}$ in the Hilbert space can be expanded as a linear combination of the eigenvectors $\{\mathbb{F}_i(z)\}$ with eigenvalues $\{E_i(\mathbf{k})\}$ of the Hamiltonian $\mathbb{H}$,

$$\mathbb{F}^{(0)}(z)=\sum_{i=1}^{N} a_i\mathbb{F}_i(z). \qquad (5)$$

The solutions can be found every time the shift parameter λ approaches one of the eigenvalues $E_l(\mathbf{k})$ provided the projection a_l is different from zero. The power m is set from the numerical precision condition chosen in each case. For other details see Refs. 19,20.

The potential profile and the probability density for the first eight hole and two electron eigenstates, at $k_{\|}=0$, for a general sample are shown in Fig. 2.

The upper part shows the first two conduction states. The ground state has eigenvalue E_1 inside the n-doped layer, whereas the second state E_2 above the bottom of the quantum well. Notice also the duplicity (spatial degeneracy) of states HH_{1+} and HH_{1-} located at the p layer on the right(+) and on left(−) barriers. The states HH_{2+} and HH_{2-} are pushed to the right(+) and to the left(−) side (interface) of the well profile, due to the presence of the n-doped layer in the conduction band (material gap preservation). Observe also that the extension (peaks) of any given hole state to the different regions of the potential profile of a sample is important, since interband transitions will depend on the selection rules plus the overlap integral between the initial and final states involved. This is an indication of the size of the coupling between layers as well as to the induced asymmetry produced to hole potential that depends on the layer separation and barrier height determining the tunneling

for each level between the regions. Certainly at large **k** values, this inter-region tunneling probability should increases. Also, this fact is important to determine the critical temperature T_c due to intraband transitions (thermal excitations), for a given *nipi*-doped sample that sets the condition for which the character of the optical conduction-valence transition can change from indirect, or recombination between states localized in the two different materials, to direct, or recombination between states localized in the same material.

The calculated energy dispersions, at $T=170$ K, for each layer in the sample number 482, is presented in Fig. 3. In order to understand the luminescence and thermal excitation in the system, we are showing the dispersions at the correct position [part (d)], where the free carriers will be traveling in the spatial potential profile.

In Fig. 3(a), we show the calculated electron dispersions for the first two states in the *n*-doped layer inside the quantum well, with the quasi-Fermi level in the first band. The wave number vector **k** is pointing along the direction shown in part (d). In part (b), we show the energy dispersions for the first two hole states on the left of the valence band of the GaAs layer. They are the states labeled HH_{2-} and LH_{2-} in Fig. 3(d). Notice that each one has multiplicity 4 due to the coupling between the four regions of confinement, occurring between levels 2 and 3 in part (d). Their wave functions should have peaks in each region of the profile and, the height of the peak is associated to the tunneling probability. The energy separation between each multiplet cannot be seen in the scale due to the large separation between the *p* layers and the center of the quantum well. Associated to this spatial multiplicity, there is also the Kramer degeneracy. In Fig. 3(c), we show the calculated dispersions of the first two hole states in the right *p*-layers, labeled as HH_{1+} and LH_{1+}. The ground state HH_{1+} (HH_{1-}) on the right (left) *p* layer have spatial multiplicity 2, since they are located between levels 3 and 4 indicated in Fig. 3(d). The level LH_{1+} has spatial multiplicity 4 and feels the presence of the V-shape potential inside the valence of the quantum well (*n* layer) in its dispersions. The same occurs for the state LH_{2-}.

In order to show this multiplicity, we have calculated the energy dispersions in the same sample, at $T=40$ K. However, we introduced a small spatial asymmetry (1 Å) in the position of the two *p*-layers. The general results are shown in Fig. 4. Parts (a–c) are the same dispersions for the states described in the previous figure (Fig. 3) and part (d) shows zoom on the dispersions spatial duplicity (2) for HH_{1+} and HH_{1-} hole states in the *p* layers as well as for the HH_{2+} and HH_{2-} states in the GaAs layer. It is clear that the closer the eigenvalue to the continuum of the valence band [between levels 1 and 2 in Fig. 3(d)] is, the larger this energy separation is, since they can tunnel more easily between the regions of confinement. Layers with large spatial separation become degenerate. In the present calculation, we have used an isolated period with two *p* layers. In multiple quantum well samples the m! ultiplicity of states certainly increases.

IV. RESULTS AND DISCUSSION

A. *n*-δ doped superlattices

The potential profile for the MQW structures containing only *n*-δ-doped layers in the QWs is shown in Fig. 5. Due to

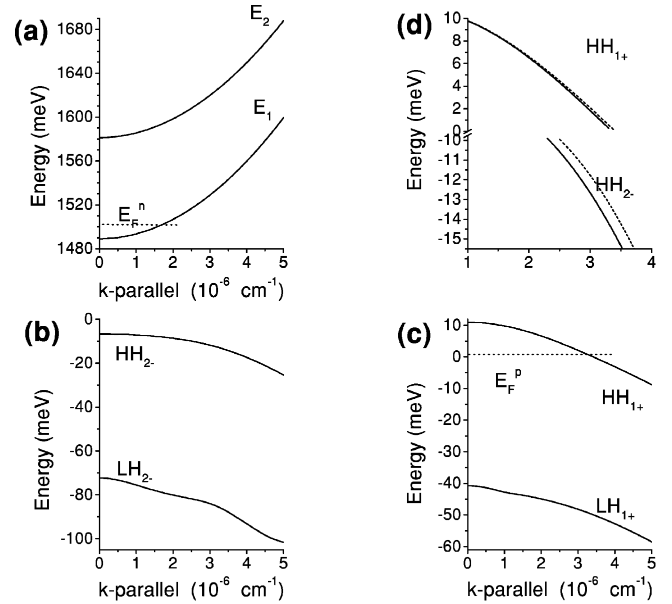

FIG. 4. Calculated energy dispersions for sample 482 at 40 K: (a) for electrons in the *n*-doped layer on the GaAs QW, (b) for hole states on the left part of valence band of GaAs QW, (c) for hole states on the right *p*-doped layer on the $Al_xGa_{1-x}As$ barrier, (d) spatial duplicity for HH_{1+} and HH_{1-} hole states in the barrier and for the HH_{2+} and HH_{2-} states in the QW.

the presence of a plane of ionized Si atoms, a V-shape potential well for electrons is introduced in the conduction band of the GaAs QW, while the valence band is divided into two half QW's. It is clear from Eq. (1) that the larger the Si concentration is, the deeper becomes the V-shape potential for an *n*-type ionized layer in the QW. In order to know how these facts will affect the MQW band gap, temperature-dependent and laser-excitation-power-dependent PL experiments were performed on three *n*-doped samples and compared to the undoped ones, used as references.

The dependence of the PL peak energy E_P on the temperature is plotted in Fig. 6, for the *n*-δ-doped MQW samples (filled symbols) and the reference or undoped sample (open squares). As the temperature increases, the measured E_P for *n*- doped and undoped samples decreases, presenting the same dependence profile which can be de-

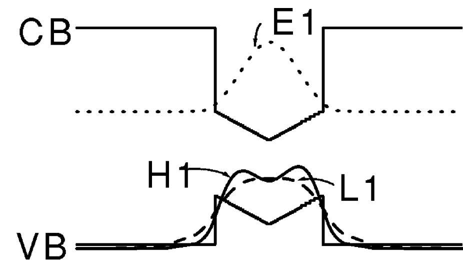

FIG. 5. Band profiles and computed probability densities for electrons and holes, for an *n*-δ-doped QW with a sheet carrier density of 1×10^{12} cm^{-2}. Dotted, solid, and dashed lines correspond to the probability density for electrons, for heavy and light holes, respectively. The calculations were performed using the effective mass model.

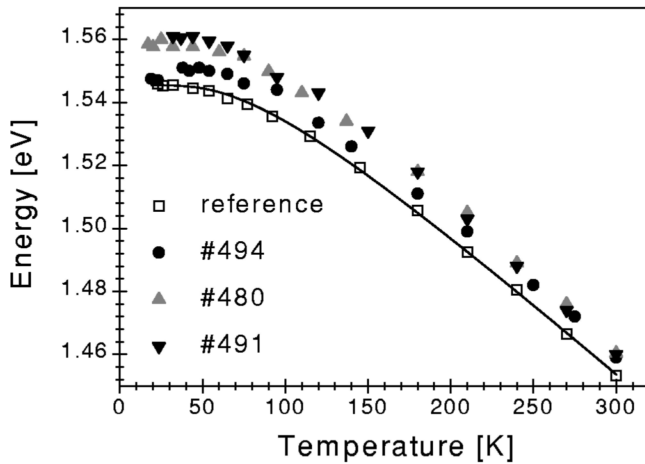

FIG. 6. PL peak energy for n-δ-doped MQW samples (represented by solid symbols) as a function of temperature. Open squares are the measurements for the reference sample, which were fitted using the semiempirical Varshni equation, represented by the solid line. The doping levels of the samples are in Table I.

scribed by the semiempirical Varshni equation. Only the fitting curve for the reference sample is displayed in Fig. 6. In this way it is easy to note that the observed PL peak energies of the doped samples are higher than those of the reference, for the entire temperature range. To better understand this behavior, the PL spectra were fitted and analyzed. The normalized 77 K PL spectra of the samples are plotted in Fig. 7. The solid line shows the PL spectrum of the undoped sample, which exhibits a relatively narrow emission line corresponding to the lowest exciton transition energy in the GaAs QW. For doped samples, the emission line is broader as well as shifted to higher energies. The spectrum of the sample with the lowest doping level, i.e., that for sample 494 is plotted

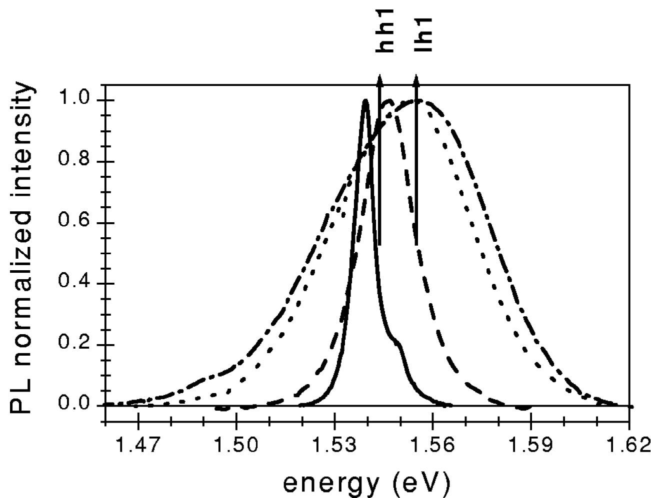

FIG. 7. 77 K normalized PL spectra of the n-δ-doped MQW samples under an excitation-power density of 44 Wcm^{-2}. The spectrum of the reference sample is represented by the solid line. Dashed, dotted, and dot-dashed lines correspond to the spectra of the n-δ-doped MQW samples labeled 494, 480, and 491, respectively. The arrows indicate the $e1-hh1$ and $e1-lh1$ transitions, which were used to fit the spectra of the doped samples.

with the dashed line. It presents a peak with energy centered 7 meV above that of the undoped sample. Since this shift corresponds to the binding energy of excitons in a 100-Å GaAs QW at 77 K,[21] it can be attributed to the quenching of excitons, as a consequence of screening effects. The peak energy is identified as the first electron-heavy-hole transition ($e1-hh1$). The other two spectra correspond to samples 480 (dotted line) and 491 (dash-dotted line), whose two-dimensional (2D) doping levels of 1.7 and 2.5×10^{12} cm^{-2}, respectively, and are almost one order of magnitude more intense than that of sample 494. The quantitative fit of both experimental PL spectra, using the sum of two Gaussian curves, suggests that their PL bands consist of two emission lines with photon energies marked by the arrows in Fig. 7. One of them is placed at the PL peak energy of sample 494, which is associated to the $e1-hh1$ transition when no excitonic interactions are present. The peak located at the highest energy corresponds to a transition involving light holes, as was calculated by solving the Schrödinger equation using the multiband effective-mass theory. As the doping level increases, the $e1-lh1$ transition is enhanced, and, therefore, the total spectrum appears slightly displaced to higher energies. This enhancement occurs due to the increase in the effective overlap between the electron and light-hole wave functions. We should stress that the QW valence band is divided into two halves, so the hole probability density corresponding to the fundamental energy level is peaked closer to the interfaces (see Fig. 5). For electrons the situation is opposite since the probability density is higher close to the center of the GaAs QW. As the doping level increases, the V-shape potential becomes deeper and consequently, the heavy-hole probability density becomes peaked closer to the GaAs/Al_xGa_{1-x}As interfaces. Since the light holes are less affected by the depth of the potential, for high doping concentrations the superposition of the electron and light hole wave functions is favored if compared to that of the electron and heavy hole.

B. *nipi*-δ-doped superlattices

Temperature-dependent and excitation-power-dependent PL experiments were performed on the *nipi*-δ-doped MQW samples. The PL peak energy as a function of temperature is displayed in Fig. 8, for samples (a) 498, (b) 502, and (c) 482. The lines are the theoretical calculations performed as described in Sec. III, while the experimental data are represented by the different symbols. Open circles correspond to the results of the reference sample and the filled triangles correspond to the *nipi* samples, all measured under an excitation-power density of 4.4 Wcm^{-2}. First, we can observe that at high temperatures the E_P of doped and undoped samples are essentially the same. However, at low temperatures E_P of the doped samples differs from that of the reference suggesting that the introduction of δ-doping layers modifies the optical properties of the MQW structure. In fact two distinct behaviors with temperature are observed in the *nipi* samples. Below a certain value defined as the critical temperature (T_c), the observed emission occurs at energies lower than the fundamental band gap, which can be identi-

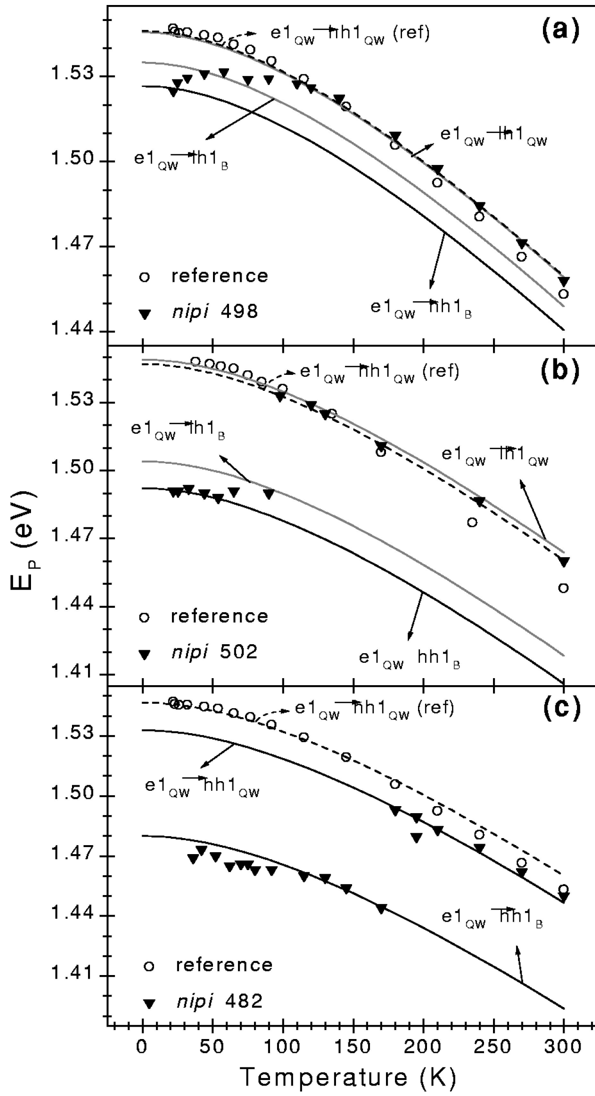

FIG. 8. PL peak energy E_P vs temperature for an excitation-power density of 4.4 Wcm^{-2}. Circles are measurements for the reference (undoped) sample, and triangles those for the; (a) 498, (b) 502, and (c) 482 *nipi*-δ-doped MQW samples. The lines are the theoretical calculations, which are explained in the text and labeled in the figure.

fied by the E_P value of the reference sample. On the other hand, above T_c, the variation of the dominant PL peak energy with temperature follows the same behavior as that of the reference sample. The value of this critical temperature is different for each sample, being lower for lower doping concentrations. From the plots, we estimated T_c to be approximately 60 K, 100 K, and 180 K for samples 498, 502, and 482, respectively, that is, the increasing values of T_c are corresponding to increasing doping concentrations.

The emission energy as a function of temperature was calculated within the full Weiler-Kane **k·p** Hamiltonian model[16] described previously. These theoretical results are included in the plots of Fig. 8, in order to identify the involved transitions. The measured E_P for the reference sample follows the first electron-heavy-hole transition in the QW ($e1_{QW}-hh1_{QW}$), represented by the dashed line. In the

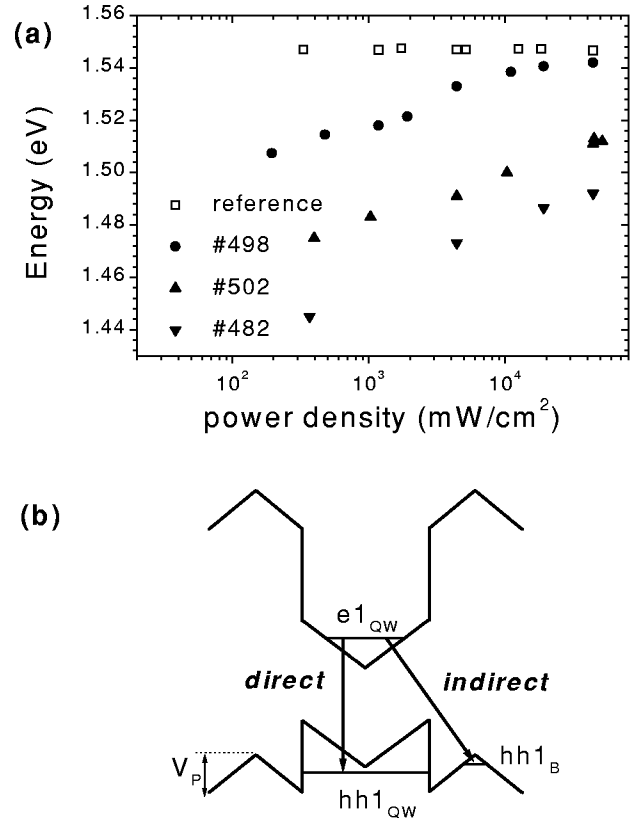

FIG. 9. (a) PL peak energy E_P vs the excitation power density. For the *nipi*-δ-doped MQW samples, represented by the filled symbols, the PL peak blue shifts as the excitation power is raised, while for the reference sample (corresponding to the open squares) no changes are observed. (b) Scheme of the potential profile for an *nipi* sample, indicating the spatially direct and indirect transitions.

nipi samples, the PL peak energies measured above T_c are also best described by the transition which involves electron and hole levels inside the GaAs QW. However, below T_c the experimental points follow the temperature behavior of the ($e1_{QW}-hh1_b$) transition, i.e., from the first electron level in the GaAs QW to the first heavy-hole level in the inverted V-shape potential in the $Al_xGa_{1-x}As$ barrier. Such a transition would be spatially indirect. Furthermore, the PL peak of the *nipi* samples shifts to higher energies with increased laser-excitation power, while that of the reference sample is unaffected, as depicted in Fig. 9(a). The blue shift is nearly linear with the logarithm of the laser power for all the *nipi* samples, with its magnitude ranging from 12 to 23 meV/decade of excitation power. This behavior could be understood as the shielding of the internal electric field by the photoinduced carriers, that increases the effective band gap which is typical for the spatially indirect transitions.[6] It should be noted that, contrary to these PL results for the *nipi* samples, for the n-δ doped structures E_P does not shift with increasing excitation power.

As found for the n-type samples, the E_P of samples 498 and 502 are higher than those for the reference, when the measurement temperature is above T_c. But for sample 482, the most heavily doped one ($n=1.82\times10^{12}$ cm^{-2} and $p=2.3\times10^{12}$ cm^{-2}), this does not happen. Indeed, this be-

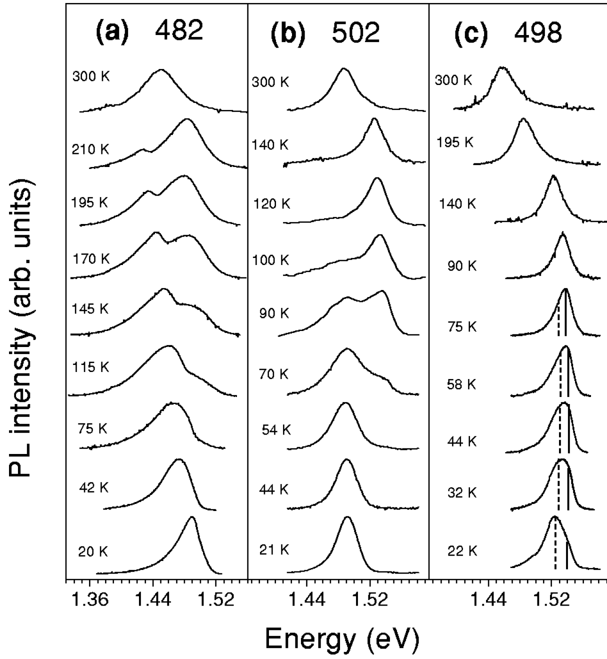

FIG. 10. PL spectra of (a) 482, (b) 502, and (c) 498 *nipi*-δ-doped samples acquired at different temperatures, under an excitation-power density of 4.4 Wcm^{-2}. Around their critical temperature, two distinct PL peaks are observed for samples 482 and 502, corresponding to the spatially indirect and direct transitions. For sample 498, these emissions can only be resolved by fitting the spectra with two Gaussians, whose maxima are indicated by the dashed and filled lines for the spatially indirect and direct transitions, respectively.

havior was previously explained under the assumption that the samples had the same MQW structure, which is not the case for samples 482 and the reference, 484. The analysis of their x-ray spectra corresponds to a 95-Å and 115-Å QW width, respectively. From calculations using the effective-mass model, we have found that the $e1-hh1$ transition, for both QW widths, agree with the PL emissions observed.

Figure 10 shows a set of PL spectra at various temperatures for samples (a) 482, (b) 502, and (c) 498. The curves were intentionally offset along the y axis with respect to each other for better clarity. At low temperatures the emission due to the indirect transition dominates. As the temperature increases approaching T_c, this PL peak is reduced in intensity and another emission at a higher energy becomes observable. For samples 482 and 502, two emissions can clearly be distinguished in their PL spectra around T_c, as it is shown in Fig. 10(a,b), respectively. They are associated to the spatially indirect and direct transitions. These two peaks cannot be resolved for the spectra of sample 498, which is the least doped one. But although its PL spectra show only one broad peak, the presence of the two emissions was confirmed by the fit with the sum of two Gaussian curves whose maxima are indicated by the vertical lines in the Fig. 10 (c). Besides, as occurs with the other two samples, an increase of the is observed around T_c due to the coexistence of the two transitions. For higher temperatures, spatially direct transitions dominate for all *nipi* samples.

TABLE II. Experimental and computed values of T_c, for an excitation power density of 4.4 Wcm^{-2}. V_P is the height of the inverted V-barrier potential.

Sample	V_P(V)	T_c^{exp} (K)	T_c^{calc} (K)
498	44	<60	16.2
502	52	100±10	89
482	98	180±10	169

From the PL results described above, T_c is interpreted as the temperature for which the nature of the transition changes from indirect to direct. It depends on the structure of the sample and on the laser-excitation power used in the PL experiment. In Table II, the experimental values of T_c are summarized. They were extracted from the plots of PL peak energy vs temperature (Fig. 8). In this table V_P represents the height of the inverted V-shape potential in the barriers, as drawn in Fig. 9(b). The V_P values were calculated using Eq. (1). We can observe that T_c increases as V_P increases, that is, T_c is higher for high p doping concentrations, according to Eq. (1). The values of T_c^{calc} included in Table II, are the estimated values of T_c, taken from the energy difference between the quasi-Fermi level in the inverted V potential, at the barriers, and the first heavy-hole level in the GaAs QW. The agreement between the estimated and the experimental results means that the change from indirect to direct transition takes place because of the hole transfer from the Al_xGa_{1-x}As barrier to the GaAs QW. When the hole energy levels in the barrier and in the QW become resonant, there is a more effective transfer of holes from the barrier to the QW, favoring the spatially direct optical transition inside the QW. Since the hole energy level in the QW depends on its doping level, T_c also depends on it. In fact, the larger the Si concentration is, the closer to the continuum become the hole levels. Therefore, the energy difference between QW and barrier hole levels will be larger as T_c increases.

As for the dependence of T_c on the excitation power, since the energy difference between well and barrier states diminishes when the laser excitation power is increased, a

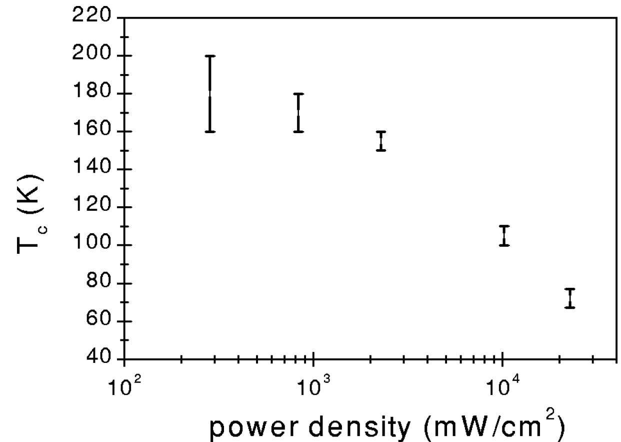

FIG. 11. Critical temperature as a function of the logarithm of incident power density, for sample, 482.

consequent reduction of T_c is expected. This power dependence is observed for all the *nipi* samples. In Fig. 11 the range of T_c values for five laser power densities are shown for sample 482. Those values were extracted from the plots of the PL peak energy vs temperature for each excitation power used, so the error bars are due to the temperature steps used in the measurements.

If the *nipi*-MQW structures are expected to be used in amplitude modulators, some requirements should be fulfilled, making the obtained results particularly useful. The introduction of a δ-doping superlattice in a MQW structure should not give rise to optical transitions within the fundamental energy gap. Therefore, when designing such modulator structures one should choose the sample parameters so as to keep T_c much lower than the device operation temperature. One should also pay attention to the power of the optical signal to be modulated since as it was shown, T_c depends on the excitation power. By these means, the only observable optical transition is the $e1_{QW}-hh1_{QW}$, which essentially coincides with that of the undoped MQW structure. It should be pointed out that no absorption below the fundamental gap was observed in preliminaries photoluminescence excitation results.

V. CONCLUSION

We have presented a photoluminescence study of GaAs/$Al_xGa_{1-x}As$ $nipi$-doped samples, where a Si δ-doping layer is placed at the center of the GaAs QW and a C δ-doping layer is placed at the center of the $Al_xGa_{1-x}As$ barriers. MQW structures with only n-δ-doped layers in the GaAs QW were also studied. The PL peak energy dependence on temperature revealed that at low temperatures, the emission occurs below the fundamental band gap and, above a certain temperature called critical temperature T_c the emission follows the same temperature trend as that of the reference. Theoretical calculations were performed to understand the dependence of the PL peak energy with the temperature. We found that the emission observed below T_c is best described by a spatially indirect transition from the first electron level in the GaAs QW to the first heavy-hole level in the inverted V-shape potential in the $Al_xGa_{1-x}As$ barrier ($e1_{QW}-hh1_b$). The PL study as a function of incident excitation power has confirmed the spatially indirect character of the transitions, which occur below T_c. Above T_c the PL emissions are best described, theoretically, by the transition between electron and hole levels within the QW, that is, spatially direct transition. The critical temperature was interpreted as the temperature at which the dominant nature of the transition changes from indirect to direct. T_c depends largely on the depth of the potential introduced by the δ layers, which, in turn, depends on sample parameters such as p- and n-δ-doping concentration, and well and barrier widths. In addition, it presents a strong dependence on the incident excitation power which changes both carrier densities.

ACKNOWLEDGMENTS

This work has been partially supported by CNPq, FAPERJ, FAPESP, CONICET, and by the Research and Development Center, Ericsson Telecomunicações S.A. of Brazil.

*Electronic address: sandra@labsem.cetuc.puc-rio.br
†On leave from Physikalisches Institut-Universitaet Stuttgart-Germany.

[1] G.H. Döhler, H. Künzel, D. Olego, K. Ploog, P. Ruden, H.J. Stolz, and G. Abstreiter, Phys. Rev. Lett. **47**, 864 (1981).
[2] C.J. Chang-Hasnain, G. Hasnain, N.M. Johnson, G.H. Döhler, J.N. Miller, J.R. Whinnery, and A. Dienes, Appl. Phys. Lett. **50**, 915 (1987).
[3] G.H. Döhler, IEEE J. Quantum Electron. **22**, 1682 (1986).
[4] P. Ruden and G.H. Döhler, Phys. Rev. B **27**, 3538 (1983).
[5] M.B. Johnston, M. Gal, G. Li, and C. Jagadish, J. Appl. Phys. **82**, 5748 (1997).
[6] S. Bastola, S.J. Chua, and S.J. Xu, J. Appl. Phys. **83**, 1476 (1998).
[7] W. Batty and D.W.E. Allsopp, IEEE Photonics Technol. Lett. **7**, 635 (1995).
[8] S.D. Koehler, E.M. Garmire, A.R. Kost, D. Yap, D.P. Docter, and T.C. Hasenberg, IEEE Photonics Technol. Lett. **7**, 878 (1995).
[9] C. Thirstrup, P. Robson, P.L.K. Wa, M.A. Pate, C.C. Button, and J.S. Roberts, J. Lightwave Technol. **LT12**, 425 (1994).
[10] A.G. Larsson and J. Maserjian, Opt. Eng. **31**, 1576 (1992).
[11] B. Jonsson, A.G. Larsson, O. Sjölund, S. Wang, T.G. Andersson, and J. Maserjian, IEEE J. Quantum Electron. **30**, 63 (1994).
[12] W. Batty and D.W.E. Allsopp, Electron. Lett. **29**, 2066 (1993).
[13] C.V.B. Tribuzy, R. Butendeich, M.P. Pires, P.L. Souza, and A.B. Henriques, J. Appl. Phys. **90**, 1660 (2001).
[14] G.M. Sipahi, R. Enderlein, L.M.R. Scolfaro, and J.R. Leite, Phys. Rev. B **53**, 9930 (1996).
[15] G.M. Sipahi, R. Enderlein, L.M.R. Scolfaro, J.R. Leite, E.C.F. daSilva, and A. Levine, Phys. Rev. B **57**, 9168 (1998).
[16] M.H. Weiler, in *Semiconductors and Semimetals*, edited by R.K. Willardson and A.C. Beer (Academic, New York, 1981), Vol. 16, p. 119.
[17] O. Band, in *Semiconductors: Physics of III-V Compounds*, edited by O. Madelung, M. Schulz, and H. Weiss (Springer-Verlag, Berlin, 1982).
[18] Z. Ikonic, R.W. Kelsall, and P. Harrison, Phys. Rev. B **64**, 125308 (2001).
[19] D.S. Watkins, *Fundamentals of Matrix Computations* (Wiley, Singapore, 1991).
[20] C. Juang, K.J. Kuhn, and R.B. Darling, Phys. Rev. B **41**, 12 047 (1990).
[21] R.L. Greene, K.K. Bajaj, and D.E. Phelps, Phys. Rev. B **29**, 1807 (1984).